

SUPPLEMENTAL INFORMATION

SYNTHESIS OF NANOPARTICLES

➤ *Synthesis of CoFe and NiFe*

Briefly, appropriate amounts of $\text{FeCl}_3 \cdot 6\text{H}_2\text{O}$ (Sigma Aldrich, ACS Reagent Grade, $\geq 97\%$) and $\text{NiCl}_2 \cdot 6\text{H}_2\text{O}$ (Sigma Aldrich, ACS Reagent Grade, $\geq 98\%$) and $\text{CoCl}_2 \cdot 6\text{H}_2\text{O}$ (Sigma Aldrich, ACS Reagent Grade, $\geq 98\%$) were added to the 100 mL ethanol/water mixture (1:4 ratio) to make the total of 0.05M $\text{FeCl}_3 \cdot 6\text{H}_2\text{O}$ and $\text{NiCl}_2 \cdot 6\text{H}_2\text{O}$ (or $\text{CoCl}_2 \cdot 6\text{H}_2\text{O}$). Subsequently, 100 mL of 0.2M NaBH_4 was added dropwise to the above solution and mixed for 30 min under Ar atmosphere. The resulting product was isolated by a magnetic rod, washed with DI water and ethanol, dried in a vacuum oven, and stored in a desiccator with continuous Ar flow.

➤ *Synthesis of CuFe*

CuFe nanoparticles with target 5 at. % and 25 at. % Cu content were prepared. Briefly, 100 mL of 0.2M NaBH_4 in deionized water was added dropwise to a solution of 0.05 M $\text{FeCl}_3 \cdot 6\text{H}_2\text{O}$ (Sigma-Aldrich) in a 100 mL ethanol/water mixture (1:4 ratio) under Ar atmosphere. The resulting ZVI product was isolated by a magnetic rod, washed with DI water and ethanol and dried in a vacuum oven. Bimetallic CuFe particles were synthesized by a surface modification of ZVI. The solutions of CuCl_2 (Sigma Aldrich, $\geq 99\%$) targeting 5 at. % and 25 at. % Cu content were slowly added to the suspension of ZVI (prepared as described above) under Ar atmosphere and vigorous stirring. The resulting nanoparticles were collected by a magnet, filtered, and washed with DI water and ethanol.

CHARACTERIZATION OF NANOPARTICLES

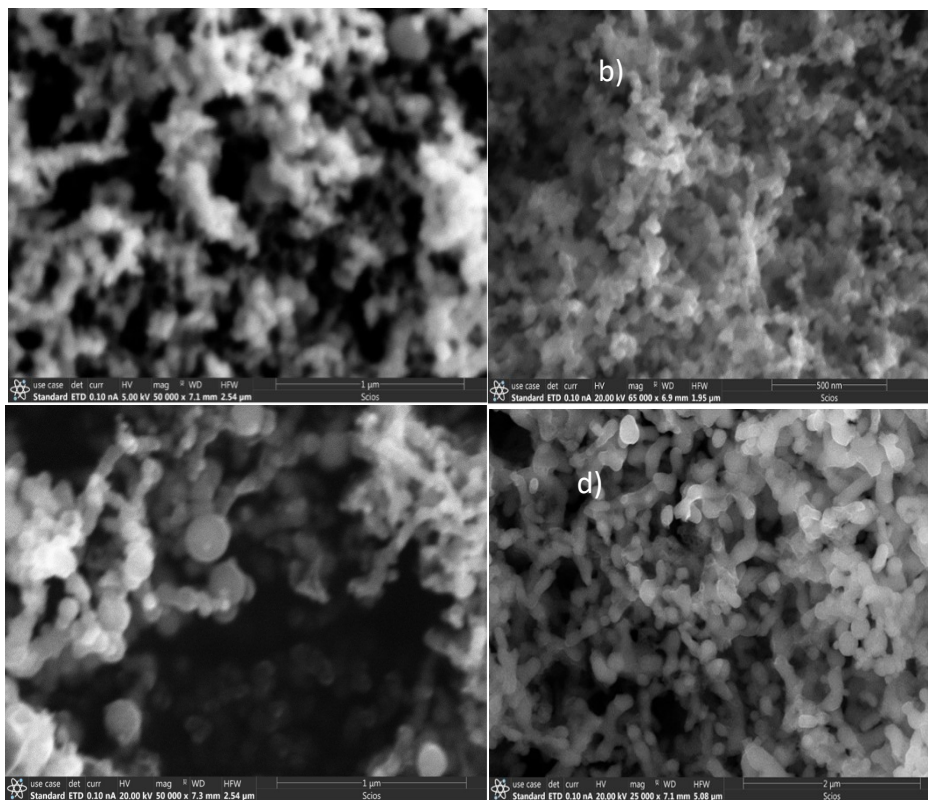


Figure S.1. SEM images of bimetallic nano ZVI: (A) 5 at. % Ni, (B) 25 at. % Ni, (C) 5 at. % Cu, and (D) 25 at. % Cu.

The scanning electron microscopy (SEM) images of bimetallic nano ZVI were taken on Scios DualBeam microscope in order to investigate the morphology and composition of synthesized bimetallic nanoparticles. Figure S.1 show the images of bimetallic nano ZVI with different Ni and Cu content. As can be seen from these images, the bimetallic particles had uniform spherical shape. The particles at higher Ni concentration (25 at. % Ni) possessed smaller average size of 50 nm, while larger particles (~100 nm) were obtained at lower Ni concentration (5 at. % Ni). A similar trend was observed for the CuFe system, where the particle size slightly decreased with increased Cu concentration: 150-200 nm for 5 at. % Cu, and 50-100 nm for 25 at. % Cu.

Table S.1. ICP-MS chemical composition of bimetallic nano ZVI.

2nd metal, at. % (target)	2nd metal, at. % (ICP-MS)
5%Ni	5.2
25%Ni	25.2
5%Cu	2.8
25%Cu	20.7
5%Co	5.3
25%Co	26.2

The morphology and structure of the bimetallic nano ZVI nanoparticles were further investigated by TEM (Fig. S.2). The content of a second metal (5 vs. 25 at. %) did not have a significant impact on ZVI particle morphology. Similar to pure nano ZVI, the bimetallic nanoparticles were spheroidal in shape (20–50 nm diameter) and aggregated into chain-like clusters. Each primary particle consisted of a well-defined dense core of the elemental Fe^0 surrounded by a continuous layer of lighter contrast, corresponding to lower density metal oxides.

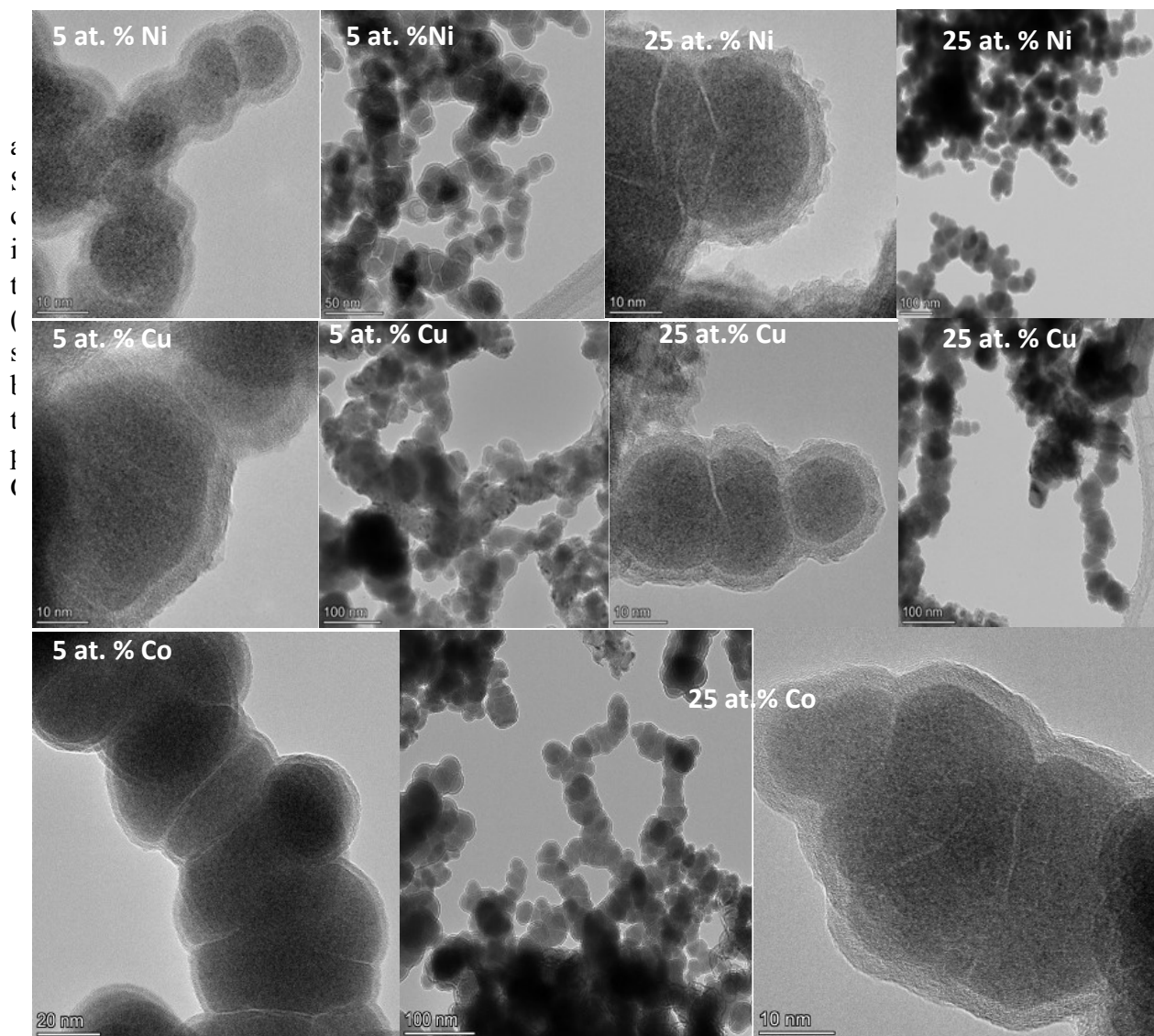


Figure S.2. HRTEM images of bimetallic nanoparticles.

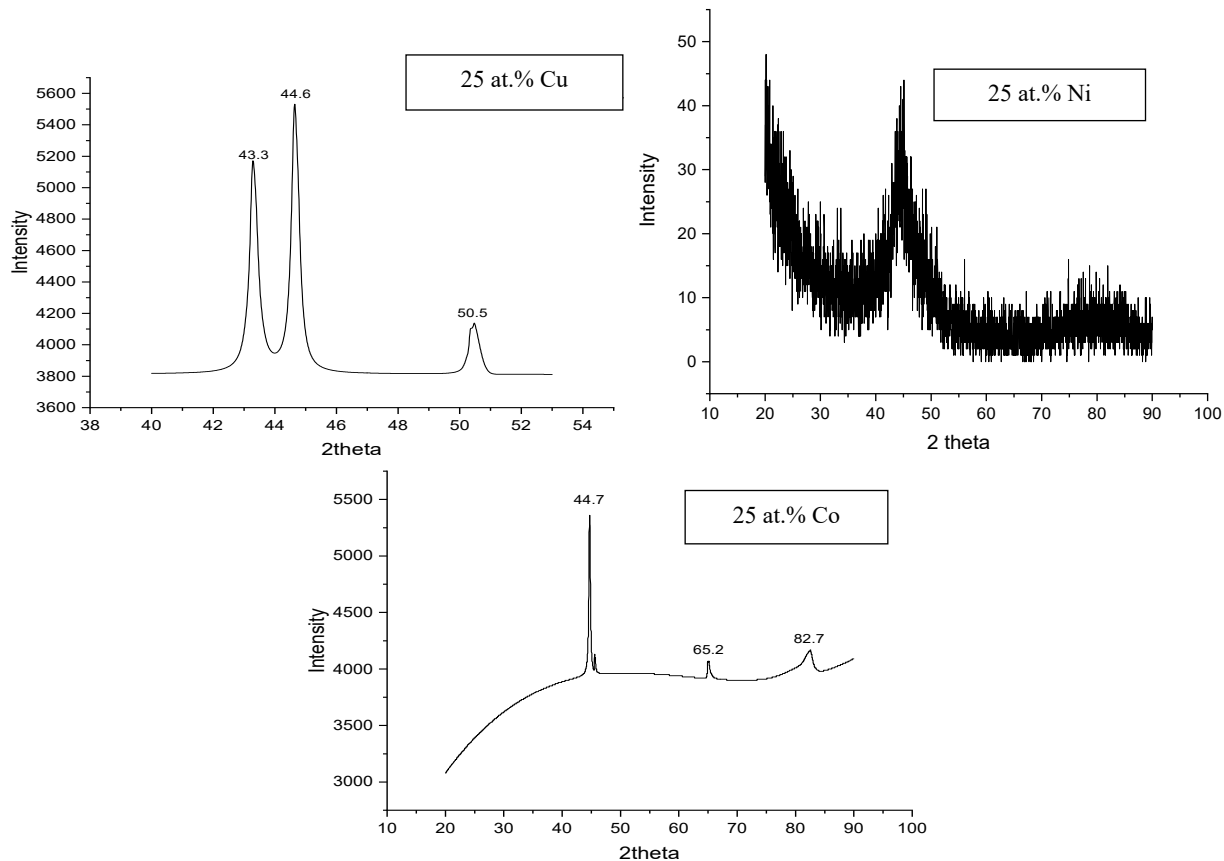


Figure S.3. XRD profiles of bimetallic ZVI nanoparticles.

The Fe 2p spectra revealed the presence of Fe⁰ as well as Fe²⁺ and Fe³⁺ oxides. The Fe⁰ peak at 706 eV was enlarged after Ar⁺ sputtering showing increased subsurface Fe⁰ content. The Ni 2p scan of the topmost surface layers showed the presence of metallic Ni⁰ at 852.6 eV and Ni²⁺ oxide at 855.9 eV. After Ar⁺ sputtering, the Ni 2p scan of the subsurface region showed the presence of elemental Ni⁰ only.

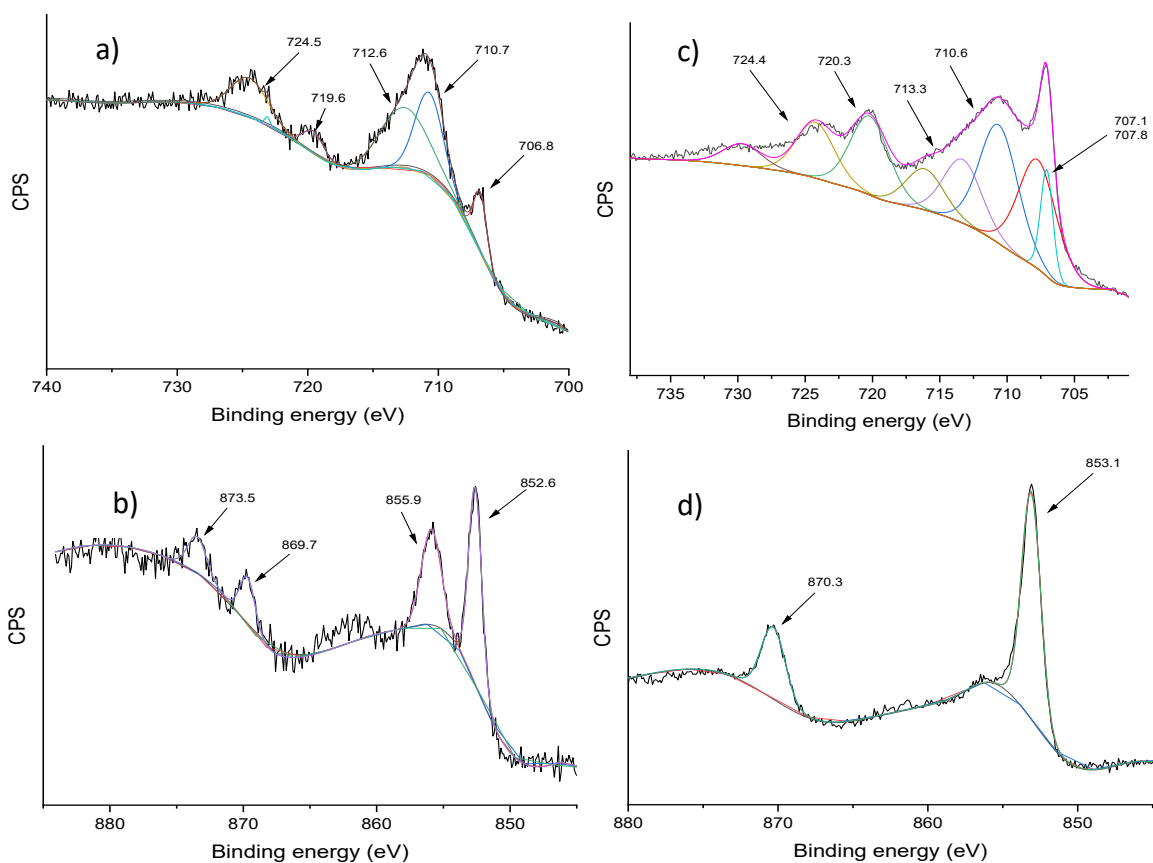


Figure S.4. XPS Fe 2p (a) and Ni 2p (b) spectra of topmost surface of bimetallic NiFe system (25 at. % Ni); and Fe 2p (c) and Ni 2p (d) spectra of subsurface region after 60 s of Ar⁺ sputtering.

Figure S.5. shows the XPS spectra of CoFe nanoparticles, i.e., the core level Fe 2p and Co 2p spectra of the topmost surface and subsurface region after Ar⁺ sputtering. Similar to other nanoparticles of this study, the Fe 2p spectra revealed the presence of Fe²⁺ and Fe³⁺ species (peaks at 710 and 712 eV) along with the small peak at 706 eV indicating the presence of elemental Fe⁰. After the removal of topmost surface layer via Ar⁺ sputtering, the Fe⁰ peak increased in intensity showing a similar core-shell structure as in nano ZVI. The sharp peaks observed in the Co 2p spectra at 788 eV and 793 eV correspond to elemental Co⁰. The intensity of Co⁰ peaks increased after the removal of the top surface layer, indicating higher concentration of elemental Co in a subsurface layer of bimetallic nanoparticles. The Co 2p spectra of top surface layers (Figure S.5b)

also showed peaks at ~ 780 and ~ 793 eV, with satellite peaks at ~ 786 eV and ~ 815 eV corresponding to the Co^{2+} oxidation state. Another set of peaks at 782 eV and 792 eV indicated the presence of Co^{3+} oxidation state. After removing the top surface layers, the peaks corresponding to Co^{3+} disappeared, indicating that the subsurface region of CoFe particles contained elemental Co^0 and Co^{2+} , while the top surface layers contained elemental Co^0 , Co^{2+} and Co^{3+} .

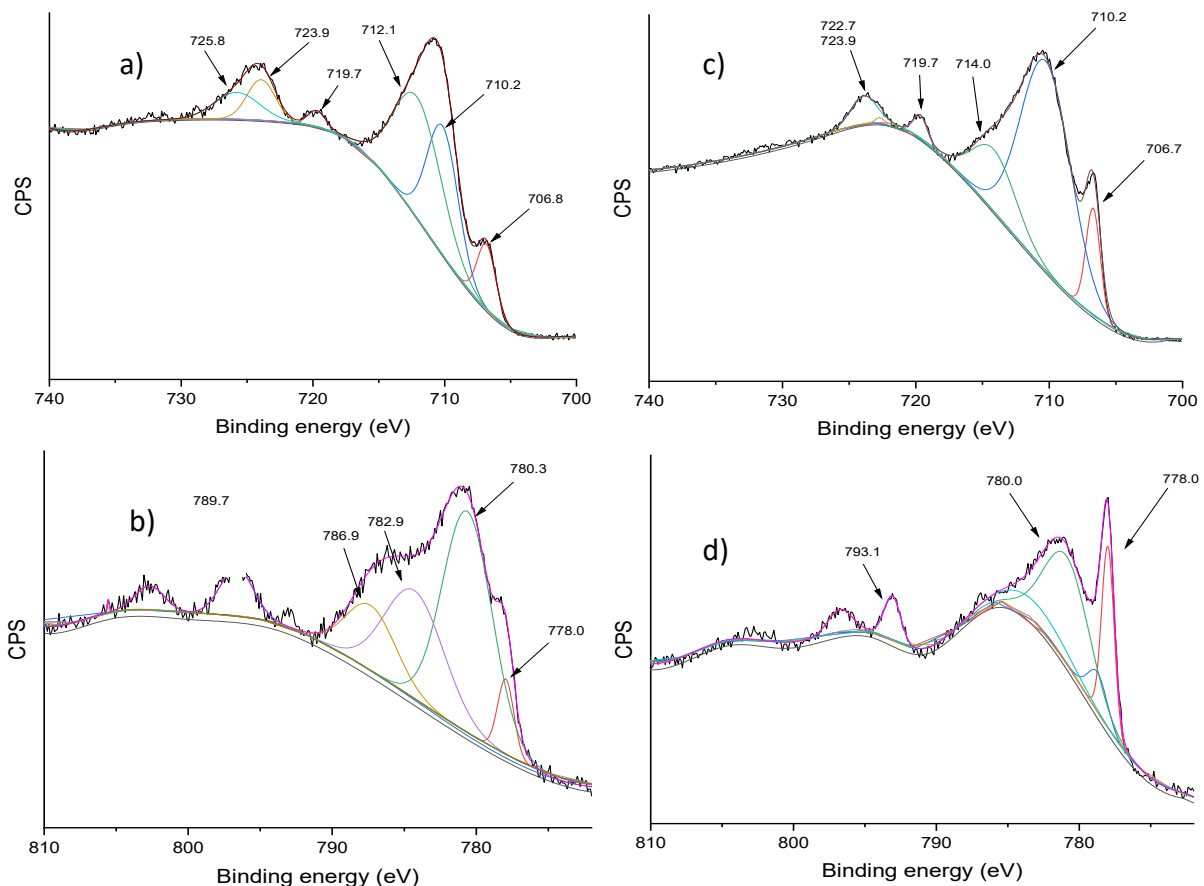


Figure S.5. XPS Fe 2p (a) and Co 2p (b) spectra of bimetallic CoFe (25 at. % Co) of particle surface and Fe 2p (c) and Co 2p (d) spectra after ion etching (60 s Ar sputtering).

Figure S.6 shows the XPS spectra of the CuFe nanoparticles. Unlike pure nano ZVI, CoFe and NiFe, the Fe 2p spectra of the top surface layers in CuFe particles showed no peaks of elemental Fe^0 . However, the Fe^0 peaks were observed after Ar^+ sputtering, indicating that elemental Fe^0 was still present in the bulk of CuFe nanoparticles. Moreover, no Fe^{3+} peaks were observed in either the top surface layers nor the subsurface region, indicating the presence of Fe^{2+} oxide only. The Cu 2p spectra of the top surface layers and subsurface region after Ar^+ sputtering exhibited similar peaks at ~ 932 and 955 eV, which were, in the absence of satellite peaks, characteristic peaks for $\text{Cu}^0 2p_{3/2}$ and $\text{Cu}^0 2p_{1/2}$, respectively.

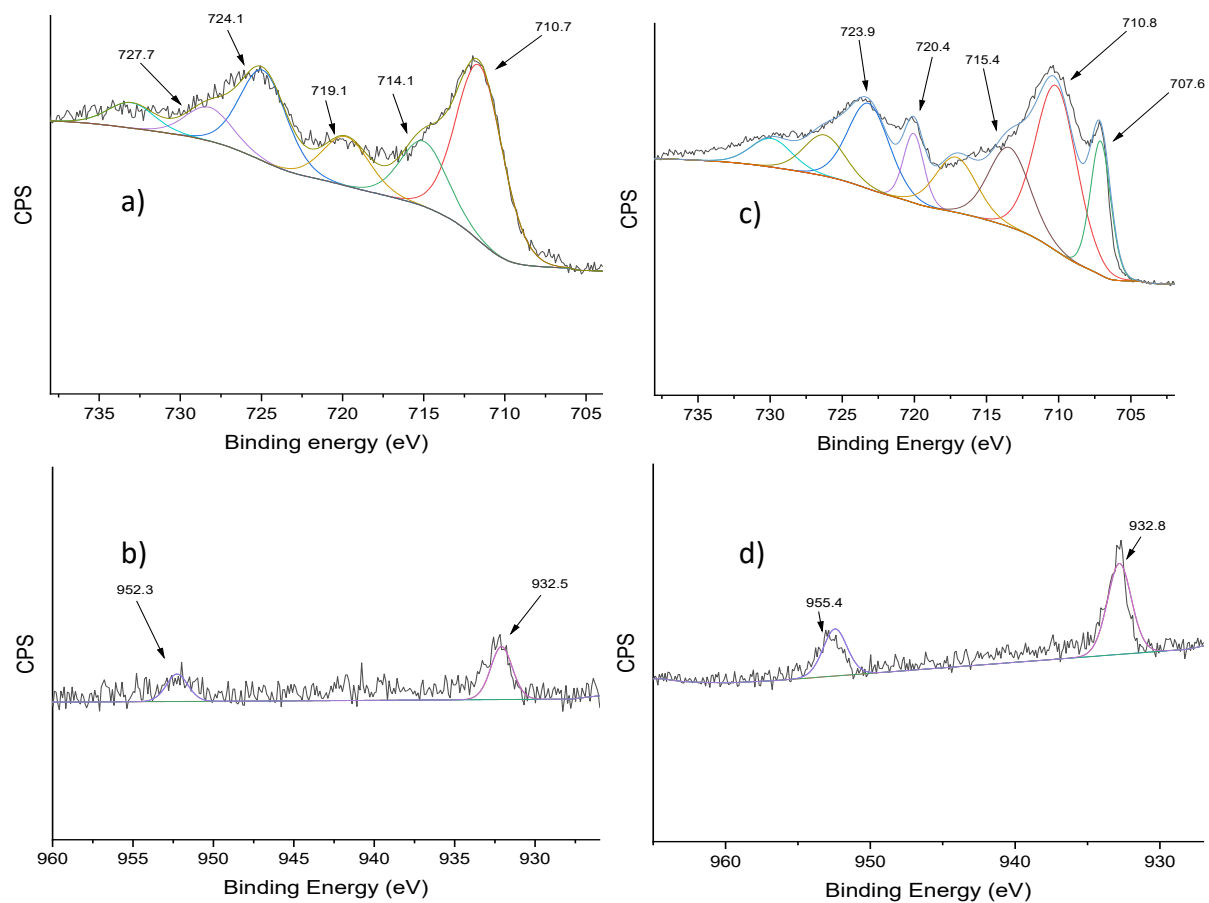


Figure S.6. XPS Fe 2p (a) and Cu 2p (b) spectra of bimetallic CuFe (25 at. % Cu) of particle surface and Fe 2p (c) and Cu 2p (d) spectra after ion etching (60 s Ar sputtering).

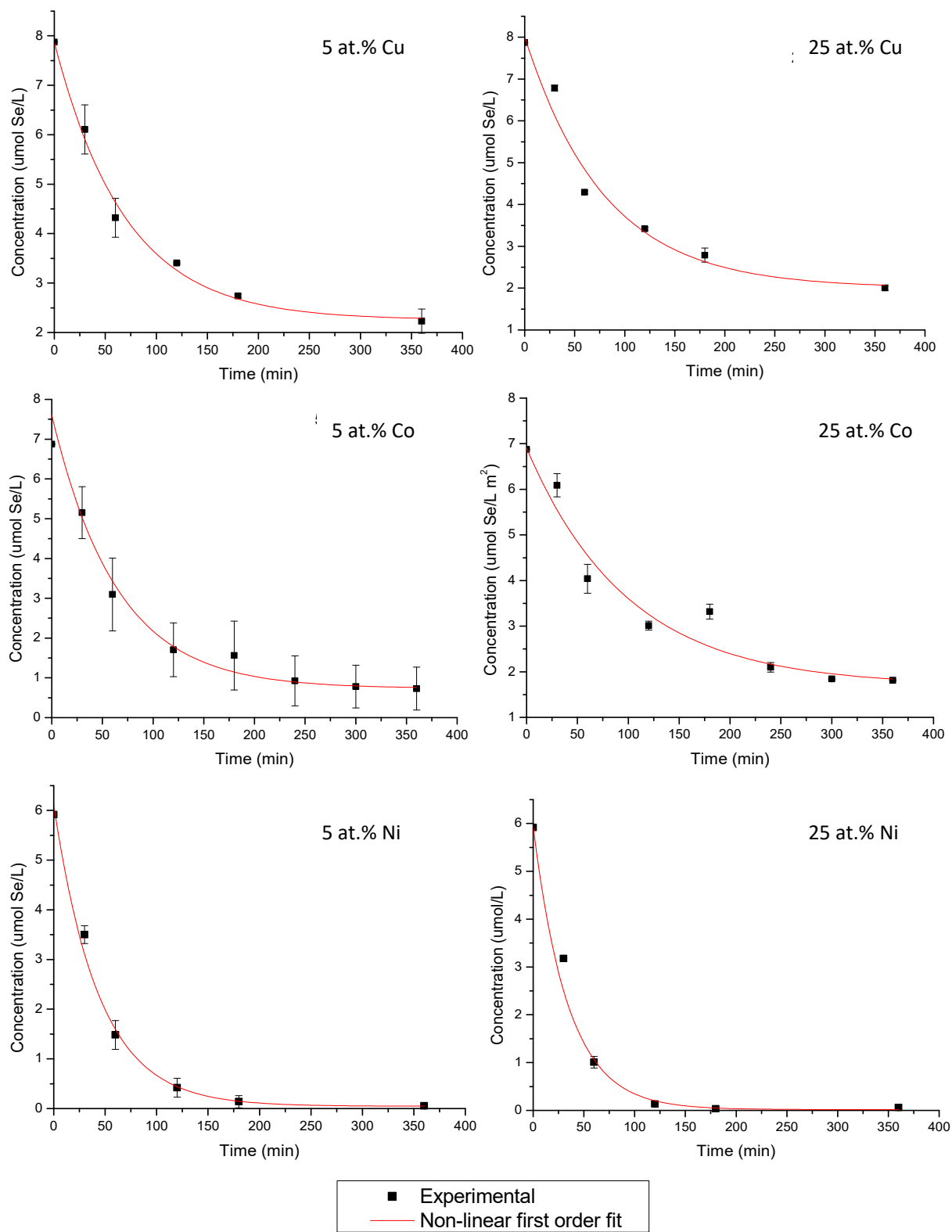


Figure S.7. Kinetics of Se^{6+} removal using bimetallic nano ZVI containing target 5 and 25 at. % of a second metal.

Selenate anions can be reduced in solution by ZVI to selenite Se^{4+} , elemental Se^0 , and selenide Se^{2-} . Insoluble Se^0 and Se^{2-} are strongly adsorbed at an interface between Fe^0 core and Fe oxide/oxyhydroxide shell (Eq S1-S3) (1-10). The reduction can be explained based on the standard oxidation-reduction potentials of the anions:



It has been shown that the removal of contaminants using ZVI can be significantly enhanced by coupling ZVI to a less reactive metal (more electropositive metal) (11). When the iron surface is covered with another metal having a higher redox potential the coupled iron and a second metal form galvanic cells in which iron serves as the anode, gets preferably oxidized, while the less reactive metal is protected and remains unchanged, acts as a catalyst, and increases the reduction rate (12). The proposed mechanisms for the reduction of pollutants by bimetallic nanoparticles suggest that during the reduction of regulated pollutants by bimetallic particles, iron, which has a negative redox potential is usually active and acts as an electron donor to reduce the pollutants, whereas a second metal with a more positive redox potential is generally inactive and drives the reduction of regulated pollutants by forming infinite galvanic cells hence improving the reactivity of Fe (13, 14).

References

- (1) Bang, S.; Johnson, M. D.; Korfiatis, G. P.; Meng, X. Chemical reactions between arsenic and zero-valent iron in water. *Water research (Oxford)* **2005**, *39*, 763-770, DOI: 10.1016/j.watres.2004.12.022.
- (2) Tang, C.; Huang, Y. H.; Zeng, H.; Zhang, Z. Reductive removal of selenate by zero-valent iron: The roles of aqueous Fe^{2+} and corrosion products, and selenate removal mechanisms. *Water research (Oxford)* **2014**, *67*, 166-174, DOI: 10.1016/j.watres.2014.09.016.
- (3) Mondal, K.; Jegadeesan, G.; Lalvani, S. B. Removal of Selenate by Fe and NiFe Nanosized Particles. *Industrial & engineering chemistry research* **2004**, *43*, 4922-4934, DOI: 10.1021/ie030715l.
- (4) Zhang, Y.; Wang, J.; Amrhein, C.; Frankenberger, W. T., Jr Removal of Selenate from Water by Zerovalent Iron. *Journal of Environmental Quality* **2005**, *34*, 487-495, DOI: 10.2134/jeq2005.0487.
- (5) Yoon, I.; Kim, K.; Bang, S.; Kim, M. G. Reduction and adsorption mechanisms of selenate by zero-valent iron and related iron corrosion. *Applied catalysis. B, Environmental* **2011**, *104*, 185-192, DOI: 10.1016/j.apcatb.2011.02.014.

- (6) Wu, J.; Zhao, J.; Li, H.; Miao, L.; Hou, J.; Xing, B. Simultaneous Removal of Selenite and Selenate by Nanosized Zerovalent Iron in Anoxic Systems: The Overlooked Role of Selenite. *Environmental science & technology* **2021**, *55*, 6299-6308, DOI: 10.1021/acs.est.0c08142.
- (7) Lien, H.; Wilkin, R. T. High-level arsenite removal from groundwater by zero-valent iron. *Chemosphere (Oxford)* **2005**, *59*, 377-386, DOI: 10.1016/j.chemosphere.2004.10.055.
- (8) Tuček, J.; Pruček, R.; Kolařík, J.; Zoppellaro, G.; Petr, M.; Filip, J.; Sharma, V. K.; Zbořil, R. Zero-Valent Iron Nanoparticles Reduce Arsenites and Arsenates to As(0) Firmly Embedded in Core–Shell Superstructure: Challenging Strategy of Arsenic Treatment under Anoxic Conditions. *ACS sustainable chemistry & engineering* **2017**, *5*, 3027-3038, DOI: 10.1021/acssuschemeng.6b02698.
- (9) Kanel, S. R.; Manning, B.; Charlet, L.; Choi, H. Removal of Arsenic(III) from Groundwater by Nanoscale Zero-Valent Iron. *Environmental science & technology* **2005**, *39*, 1291-1298, DOI: 10.1021/es048991u.
- (10) Bang, S.; Johnson, M. D.; Korfiatis, G. P.; Meng, X. Chemical reactions between arsenic and zero-valent iron in water. *Water research (Oxford)* **2005**, *39*, 763-770, DOI: 10.1016/j.watres.2004.12.022.
- (11) O'Carroll, D.; Sleep, B.; Krol, M.; Boparai, H.; Kocur, C. Nanoscale zero valent iron and bimetallic particles for contaminated site remediation. *Advances in water resources* **2013**, *51*, 104-122, DOI: 10.1016/j.advwatres.2012.02.005.
- (12) Scaria, J.; Nidheesh, P. V.; Kumar, M. S. Synthesis and applications of various bimetallic nanomaterials in water and wastewater treatment. *Journal of environmental management* **2020**, *259*, 110011, DOI: 10.1016/j.jenvman.2019.110011.
- (13) Wu-Jun Liu, Ting-Ting Qian, Hong Jiang Bimetallic Fe nanoparticles: Recent advances in synthesis and application in catalytic elimination of environmental pollutants. *Chemical Engineering Journal* **2014**, *236*, 448-463.
- (14) Chun, C. L.; Baer, D. R.; Matson, D. W.; Amonette, J. E.; Penn, R. L. Characterization and Reactivity of Iron Nanoparticles prepared with added Cu, Pd, and Ni. *Environmental science & technology* **2010**, *44*, 5079-5085, DOI: 10.1021/es903278e.